INSTITUTE OF PHYSICS PUBLISHING PLASMA SOURCES SCIENCE AND TECHNOLOGY

Plasma Sources Sci. Technol. **12** (2003) 8–21 PII: S0963-0252(03)55523-2

Breakdown processes in metal halide lamps

Brian Lay[1,3], **Richard S Moss**[2], **Shahid Rauf**[1,4] **and Mark J Kushner**[1,5]

[1] Department of Electrical and Computer Engineering, University of Illinois, 1406 W. Green St., Urbana, IL 61801, USA
[2] Department of Mechanical and Industrial Engineering, University of Illinois, 1406 W. Green St., Urbana, IL 61801, USA

E-mail: mjk@uiuc.edu

Received 13 May 2002, in final form 22 October 2002
Published 6 December 2002
Online at stacks.iop.org/PSST/12/8

Abstract

Metal halide lamps typically have cold fills of tens to a few hundred Torr of a rare gas and the vapour from the dosing of a metal halide solid and mercury. Breakdown and starting of the lamp occurs following application of multi-kV pulses across electrodes separated by a few centimetres. Restarting of warm lamps is often problematic as the available voltage is insufficient to break down the higher pressure (>many atm) of metal halide vapour. In this paper, fundamental processes during breakdown in cold and warm, idealized metal halide lamps in mixtures of Ar and Hg are investigated using a two-dimensional fluid model for plasma transport. We find that the capacitances of the walls of the discharge tube and adjacent ground planes are important in determining the breakdown voltage and avalanche characteristics. The prompt capacitance represented by, for example, external trigger wires provides a larger E/N to sustain ionization early in the avalanche. This effect is lost as the walls charge and shield the plasma from the ground planes. More rapid breakdown occurs in slightly warm lamps having small vapour pressures of Hg due to the resulting Penning mixture. Warmer lamps, having larger mole fractions of Hg, have less efficient breakdown as the increase in momentum transfer of the electrons is not offset by the additional ionization sources of the Penning mixture.

1. Introduction

Although metal halide lamps typically operate in the steady state as multi-atmosphere thermal arcs, during their starting phase the lamps are moderate pressure glow discharges [1–8]. Typical starting conditions for commercial metal halide lamps are a fill of a rare gas such as argon at tens to a few hundred Torr and the vapour pressure of the metal halide dose and/or mercury. The inter-electrode gap is 1–5 cm depending on the lamp wattage and application. The lamp envelope is usually fused silica (quartz) in larger lamps or polycrystalline alumina in smaller, higher temperature lamps. At room temperature at start-up, the metal dose, at best, provides a few to tens of milliTorr of vapour. However, during a warm restart of a lamp, the metal halide vapour pressure may be hundreds of Torr to many atmospheres. It is this high metal (or metal halide) vapour pressure which makes it difficult to restart warm lamps as the E/N (electric field/gas number density) available from the lamp ballast is typically insufficient to produce breakdown while the cathode temperature is too low for thermal emission [9, 10].

Improving the reliability and reducing the breakdown voltage for starting metal halide lamps is of great interest. Large starting voltages result in higher rates of sputtering of the cathode which ultimately reduces the lifetime of the lamp. Lower starting voltages also translate into simpler power supply ballasts. In many commercial lamps, small

[3] Present address: Sun Microsystems, 5 Omni Way, UCHL05-1116, Chelmsford, MA 01824, USA.
[4] Present address: Motorola, Inc., 3501 Bluestein Blvd, MS K-20, Austin, TX 78721, USA.
[5] Author to whom correspondence should be addressed.

amounts of radioactive isotopes, such as ^{85}Kr, are used to provide background ionization to aid in initiation of breakdown. Manufacturers are quite motivated to eliminate these radioactive additives. Finally, for a given available voltage from a power supply or lamp ballast, lowering the E/N required for breakdown increases the largest gas density for which breakdown can be achieved, thereby improving the restart capabilities of warm lamps.

The starting processes of metal halide lamps have been studied with the intent of improving reliability and restart capability [2–6]. The ignition process is typically separated into five stages: two breakdown phases, cold cathode, glow-to-arc transition and thermionic arc. The breakdown consists of two phases, the statistical time lag and the formative time lag. The formative lag time, usually a function of geometry and E/N, is the time required to avalanche the gas to a conductive state. This is usually short compared to the statistical lag time, which is the mean time for the production of seed electrons in the arc tube to initiate the avalanche. These seed electrons are typically generated by cosmic rays, photo-ionization from artificial sources such as ultraviolet (UV) flashlamps or electric emission from microscopic roughness on the tips of the cathode. Following breakdown the lamp either enters a cold cathode or a glow discharge phase. If mercury has previously condensed on the electrodes, then the lamp first enters a cold cathode phase. During this phase, ions accelerated by the large electric fields near the electrodes vaporize the mercury, which is then rapidly ionized by electrons. This 'prompt' ionization decreases the impedance of the lamp. The decrease in impedance may be temporary, though, because the source of mercury is quickly depleted. At such a time, a conventional glow discharge is established [6].

After the mercury released from the electrodes is depleted, further increases in current require an increase in the impedance of the lamp to facilitate larger E/N to sustain avalanche in the higher ionization potential buffer gas. The primary source of electrons during this period is secondary emission from the electrodes by ion bombardment. The relatively high operating voltage produces energetic ions, which both sputter the cathode and heat it. This heating eventually raises the temperature of the cathode to a sufficiently high value that thermionic emission starts, which is the beginning of the glow-to-arc transition [7, 8].

Reducing the breakdown voltage is advantageous for reducing sputtering of the cathode which results in darkening of the arc tube [4, 9]. Electronic ballasts [10] may help alleviate sputtering by regulating the breakdown voltage to an optimized waveform. Other strategies to reduce the required starting voltage (and hence sputtering) is to provide auxiliary sources of ionization. To this end some metal halide lamps include a trigger electrode adjacent to the cathode. By applying a smaller voltage between the main electrode and the trigger electrode to create a local plasma, pre-ionization is achieved with minimal sputtering. This in turn permits smaller voltages to be applied between the two main electrodes and still ensure breakdown.

More recently, small UV sources [1, 2] have been positioned within the glass shroud that encloses the lamp to produce free electrons by either photoemission from the cathode or arc tube or by photo-ionization of metal vapour. Zaslavsky *et al* [1], and Byszewski and Budinger [2] investigated the time it takes for lamps to break down with and without a UV source. The addition of a UV source was found to reduce the statistical time lag by providing a reliable external source of free electrons.

Many approaches to the restart of warm, high pressure arc-tubes have been investigated [5]. Electronic ballasts make it possible to detect the hot reignition phase and, thus, apply a larger voltage to the lamp to ensure breakdown. Depending on the gas pressure though, this might not be feasible. Lamps that require in excess of 20–30 kV for reignition pose the risk of external arcing and need special sockets that can withstand these higher voltages. Another approach is to turn the lamp off slowly. By maintaining a small current through the lamp, the impedance of the lamp can be maintained in a low state. A full discharge can then be restored quickly by simply increasing the ballast to full power [11, 12].

In this paper, results from a two-dimensional plasma transport model will be used to investigate fundamental issues in lamp starting. The intent of this work is to provide insight into possible design rules that might be applied to the improvement of start-up in moderate pressure, metal halide lamps. We will discuss breakdown and the onset of a glow discharge, as opposed to a cold cathode discharge, as evaporation of mercury from the cathode is not addressed. Our results suggest that the combined capacitance of the lamp envelope and surrounding structures is important in determining the minimum breakdown voltage for a given gas fill. Similar to streamer propagation, photo-ionization plays an important role in advancing the ionization front. Moderate pressures of the metal vapour reduce breakdown voltages by virtue of providing a low ionization potential constituent and providing the means for a Penning gas mixture. This advantage is lost when the increased momentum transfer collision frequency wrought by the metal vapour is sufficiently large to reduce the electron temperature. The model will be described in section 2 followed by a discussion of our results for starting of lamps with internal trigger electrodes in section 3 and with external trigger electrodes in section 4. Concluding remarks are given in section 5.

2. Description of the model

The model used in this investigation, LAMPSIM, is a multi-fluid hydrodynamics simulation in which transport equations for all charged and neutral species and Poisson's equation are integrated as a function of time. Our interest is in the fundamental processes leading to breakdown during which the total energy deposition is small. We therefore address the transport of charged particles, radicals and photons, and diffusive transport for neutrals while not considering gas heating and the hydrodynamic motion of the neutral gas resulting from temperature gradients. The numerical grid uses a boundary fitting, unstructured mesh with triangular elements. The method of solution uses time-slicing between charged particle transport and neutral particle transport updates. The time evolution of charged particle densities and surface charges are solved simultaneously with Poisson's equation using an implicit Newton's method. This update is then followed with an implicit update of neutral particle densities.

The numerical mesh for LAMPSIM was produced using SkyMesh2 [13], a commercially available mesh generator. The mesh consisted only of triangles, using mesh relaxation techniques to optimize angles close to 60° and eliminate obtuse angles wherever possible. The mesh is not dynamically varied during execution of the model. The resolution of the mesh was selected to resolve both geometrical structures and regions of large electric field gradients or large particle density gradients with a fine mesh while using a coarse mesh in the outlying regions. For the cases discussed here, the mesh consisted of approximately 10 000 nodes, of which about 6000 are in the plasma regions. The differential equations discussed below were discretized using finite volume techniques. The material properties that are specified for node and volume elements which are not plasma are electrical conductivity, permittivity, temperature, optical transmission, work function, surface roughness and secondary electron emission coefficients.

The fundamental algorithms employed for plasma transport in LAMPSIM are based on those described in [14]. The charged particle update step consists of solving a set of simultaneous partial differential equations for the densities of all charged species (electrons and ions), the charge density (surface charge densities and charge density in materials) and the electric potential. Although tracking both the charge density and, separately, the density of charged species is a bit redundant, it turns out to be convenient in our method of solution. The fundamental transport equations we solved are

$$-\nabla \cdot (\varepsilon \nabla \Phi) = \sum_{j=1}^{n} q_j N_j + \rho \tag{1}$$

$$\frac{\partial N_i}{\partial t} = -\nabla \cdot \left(-D_i \nabla N_i + \frac{q_i}{|q_i|} \mu_i N_i \nabla \Phi \right) + S_i = -\nabla \cdot \phi_i + S_i \tag{2}$$

$$\frac{\partial \rho}{\partial t} = \left[\sum_{j=1}^{n} q_j [-\nabla \cdot \phi_j + S_j] - \nabla \cdot (\sigma(-\nabla \Phi)) \right]_{\mathrm{m}} \tag{3}$$

where ε, Φ, q, N, ρ, D, μ, S and σ are the permittivity, electric potential, elementary charge, species number density, charge density, diffusion coefficient, mobility, source function due to collisions and conductivity of solid materials, respectively. The subscript denotes identity of the species. ϕ is the species flux accounting for both drift in the electric field and diffusion due to density gradients. n is the total number of charged gas species (electrons and ions). These expressions are Poisson's equation (equation (1)), continuity for charged species (equation (2)) and continuity for charges on surfaces and in materials (equation (3)). The source function in equation (2) includes the gain and loss terms due to gas phase reactions (neutral chemistry, ion-molecule reactions and electron impact processes) and contributions associated with wall chemistry, including electron emission from surfaces. The brackets and subscript m in equation (3) denote that ρ is only computed on surfaces and in bulk materials.

The flux terms ϕ were formulated using the method of Scharfetter and Gummel [15]. In this method, the flux $\phi_{i+1/2}$ between density mesh points $(i, i+1)$ separated by a distance Δx is given by

$$\phi_{i+1/2} = \frac{\alpha \bar{D}(n_{i+1} - n_i \exp(\alpha \Delta x))}{(1 - \exp(\alpha \Delta x))} \tag{4}$$

where

$$\alpha = -q\bar{\mu} \left(\frac{\Phi_{i+1} - \Phi_i}{\Delta x} \right) \tag{5}$$

and $\bar{D}$ and $\bar{\mu}$ are the average diffusion coefficient and mobility in the interval. This method has the property of being upwind (or downwind) in accordance with the direction and magnitude of the drift flux compared to the diffusion flux.

All Laplacian operators are formulated using conservative finite volume techniques. For example, for node i and flux ϕ,

$$-\nabla \cdot \phi_i = -\frac{1}{V_i} \sum_{k=1}^{n} \frac{A_{i,k} \phi_{i,k}}{|\vec{r}_i - \vec{r}_k|} \tag{6}$$

where $\phi_{i,k}$, the flux between nodes i and k, is defined as being positive if directed away from i, $\vec{r}_i$ is the spatial location of node i, $A_{i,k}$ is the area of the face between the volume cells centred on nodes i and k, and V_i is the volume of the cell for node i.

The system of equations for charged particle transport and Poisson's equation are integrated in time using an implicit Newton's method. The variables at time $t + \Delta t$ are obtained from

$$A(t + \Delta t) = A(t) + \frac{\partial A}{\partial t} \Delta t = A(t) + \Delta A \tag{7}$$

where A represents the potential, density or surface charge variables at each node. Newton iterations are used to determine the ΔA values. Equations (1)–(3) are rewritten in terms of three new functions, F_1, F_2 and F_3, respectively:

$$F_1 = \nabla \cdot (\varepsilon \nabla \Phi) + \sum_{j=1}^{n} q_j N_j + \rho = 0 \tag{8}$$

$$F_2 = \frac{\partial N_i}{\partial t} + \nabla \cdot \vec{\phi} - S = 0 \tag{9}$$

$$F_3 = \frac{\partial \rho}{\partial t} - \sum_{j=1}^{n} q_j [-\nabla \cdot \phi_j + S_j] + \nabla \cdot (\sigma(-\nabla \Phi)) = 0 \tag{10}$$

These functions are linearized using a first-order Taylor series expansion:

$$\sum_k \frac{\partial F_1}{\partial \Phi_k} \Delta \Phi_k + \frac{\partial F_1}{\partial \rho_k} \Delta \rho_k + \sum_i \frac{\partial F_1}{\partial N_{i,k}} \Delta N_{i,k} = -F_1 \tag{11}$$

$$\sum_k \frac{\partial F_2}{\partial \Phi_k} \Delta \Phi_k + \sum_i \frac{\partial F_2}{\partial N_{i,k}} \Delta N_{i,k} = -F_2 \tag{12}$$

$$\sum_k \frac{\partial F_3}{\partial \Phi_k} \Delta \Phi_k + \sum_i \frac{\partial F_3}{\partial N_{i,k}} \Delta N_{i,k} = -F_3 \tag{13}$$

where the sum over k is for the local and neighbouring nodes, which are linked through the finite volume algorithms and the second sum is over species i. The Jacobian elements are numerically derived by perturbing the independent variable and re-evaluating the functions. The resulting system of equations is expressed in matrix form as $\bar{M} \cdot \bar{X} = \bar{B}$ where the matrix M consists of the Jacobian elements, the array X are the ΔA values and the array B consists of the values of the F functions. An initial estimate is made for the ΔA values

using $(\Delta t/(t - t_p))(A(t) - A(t_p))$ where t is the current time and t_p is the time of the previous update and the F functions are computed based on these values. The partial derivative in the F functions are approximated by $(A(t + \Delta t) - A(t))/\Delta t$. The matrix is solved, the F functions are updated using $A(t + \Delta t) = A(t) + \Delta A$ and the process is repeated, updating the Jacobian elements, until $F < \varepsilon$, where ε is the specified tolerance. If the back average of the number of Newton iterations required to obtain $F < \varepsilon$ is less than a specified number, usually 3, the time-step is increased. If a larger number of iterations is required, the time-step is decreased. The sparse matrix resulting from equations (11)–(13) was solved using the numerical package *dslucs*, obtained from the SLAP Sparse Matrix Library [16, 17]. The matrix solver uses a biconjugate gradient spare matrix solution technique with incomplete LU factorization for preconditioning.

In a time-splicing manner, following updates of the charged particle densities, the neutral particle densities are next implicitly updated using the expression

$$N_i(t + \Delta t) = N_i(t) - \nabla \cdot (-D_i \nabla N_i(t + \Delta t)) + S_i \qquad (14)$$

Equation (14) is sequentially solved for each species using the method of successive over-relaxation (SOR) with the Laplacian terms formulated using finite volume techniques.

Electron impact rate coefficients and transport coefficients were obtained by one of two methods. The first used the local field approximation. In that method, all electron transport coefficients are functions of the local value of E/N. The dependence of transport coefficients on E/N was derived by solving Boltzmann's equation using a two-term spherical harmonic expansion for a wide range of values for E/N [18]. A look-up table of the resulting transport coefficients was constructed and interpolated during execution of the model.

The second method was to solve the electron energy conservation equation. The equation we solved for average electron energy ε was

$$\frac{\partial(n_e\varepsilon)}{\partial t} = \vec{j} \cdot \vec{E} - n_e \sum_i N_i \kappa_i - \nabla \cdot \left(\frac{5}{2} \varepsilon \vec{\phi}_e - \lambda \nabla T_e \right),$$
$$\vec{j} = q\vec{\phi}_e \qquad (15)$$

where T_e is the electron temperature (defined as $(2/3)\varepsilon$), n_e is the electron density, κ_i is the rate coefficient for power loss (eV cm^3 s^{-1}) for collisions of electrons with species i having density N_i, λ is the electron thermal conductivity and ϕ_e is the electron flux (obtained from equation (4)). This equation is implicitly solved as a time integration using a SOR technique. An electron temperature of 0.05 eV is assigned to all surfaces in contact with the plasma and the thermal conductivity is assigned appropriate values across the sheath commensurate with the electron density in the sheath. This effectively results in an adiabatic boundary condition. The electron transport coefficients and rate coefficients for use in solving equation (15) are obtained by solving Boltzmann's equation for the electron energy distribution (EED) using a two-term spherical harmonic expansion, as when using the local field approximation. Boltzmann's equation is parametrized over a range of E/N, and a table of transport coefficients as a function of ε is constructed. This table is then interpolated during solution of equation (15).

At the pressures of interest (50–100 Torr) the electron collision frequency is $\approx 10^{10}$ s^{-1} whereas timescales for transport of charged species during lamp starting is tens to hundreds of nanoseconds (or longer) and the rate of change in applied voltage is of the order of tens of nanoseconds or longer. The EED is therefore in quasi-equilibrium with the electric field. Extensive comparisons were made between use of the electron energy equation and the local field approximation, and few differences were found. We therefore used the local field approximation for the results reported here.

Surface chemistry is included using a flux-in/flux-out boundary condition. For each species, a 'disappearance' coefficient α_i and production coefficients $\beta_{i,k}$ are specified where α_i is the probability that species i is consumed by the surface and $\beta_{i,k}$ is the rate of production of species k by species i. The returning flux from the surface is, then,

$$\phi_i = \phi_i^0(1 - \alpha_i) + \sum_k \phi_k^0 \beta_{k,i} \qquad (16)$$

where ϕ_i^0 is the flux into the surface obtained assuming the surface density is zero and the sum is over other species. When applicable, $\beta_{i,k}$ may be a function of energy of the incident particle, as in ion induced desorption or sputtering [19]. The coefficient for secondary electron emission used here was 0.1 for all ions and 0.05 for excited states having energies greater than the work function.

The value of $\beta_{i,k}$ in equation (16) includes secondary electron emission by charged and neutral species but not electric field emission. Electron production by this mechanism is included in the source function in equation (2) as being an 'external' source of electrons into the plasma which is, to first order, independent of the flux of species to the surface. Although electric field emission is not expected to be important during continuous operation of a lamp, surface roughness which produces high electric fields may produce seed electrons which enables breakdown. The electron current density due to field emission is [20]

$$j_e = AT_S^2 \exp\left(\frac{-(\Phi_W - (q^3 \eta E_S/\varepsilon_0)^{1/2})}{kT_S} \right) \qquad (17)$$

where T_S is the surface temperature, A is the Richardson–Dushman constant (120 A K^{-2} cm^2), Φ_W is the material work function and η accounts for local surface roughness that may produce electric field enhancement but is not resolved by the mesh.

Radiation transport is included as a photo-ionization mechanism to both seed the plasma with electrons and to advance the ionization front. In our model, the ionization source for species k at location $\vec{r}$ resulting from emission of photons by species j is

$$S_{k,j}^p(\vec{r}) = N_k(\vec{r}) \int N_j(\vec{r}')\sigma_{k,j} G_j(\vec{r}', \vec{r})\, d^3\vec{r}',$$
$$G_j(\vec{r}', \vec{r}) = \frac{\exp(-|\vec{r}' - \vec{r}|/\lambda_j)}{4\pi|\vec{r}' - \vec{r}|^2} \qquad (18)$$

where the densities of the species are N, and $\sigma_{k,j}$ is the photo-ionization cross section of species k by the photon generated by species j. The Green function $G_j(\vec{r}', \vec{r})$ accounts for radiation transport from $\vec{r}'$ to $\vec{r}$ with absorption length λ_j. $G_j(\vec{r}', \vec{r})$

also accounts for physical obstructions and view angles which might block the radiation. In practice $G_j(\vec{r}', \vec{r})$ is computed only for a specified volume around $\vec{r}'$, typically having a radius of 4λ–5λ. For the Ar/Hg reaction mechanism investigated here, resonance radiation from Ar(4s) was the photo-ionization source having an effective absorption length of $\lambda_j = 500\,\mu$m. The photo-ionization cross section for Hg was approximated as $\sigma_{k,j} = 50\,\text{A}^2$.

A simple circuit model is employed to provide driving voltages. The electric potential boundary conditions for the solution of Poisson's equation are obtained from the circuit model and are applied to biased metal surfaces. Each metal surface is connected to ground through a simple electrical circuit consisting of a series resistor, capacitor, inductor and power supply. The voltage waveform of the power supply is specified. Currents through each leg of the circuit are obtained by summing charged particle fluxes and displacement current obtained by time differencing the electric field at the surface. Electrically floating metal surfaces are actually represented by dielectrics having sufficiently high conductivities and permittivities that they appear to be equipotential surfaces.

For the purposes of quantifying when breakdown occurs, a 10 kΩ resistor is in series with the anode. Breakdown is signified when the current through the anode is sufficient to produce a voltage drop across the series resistor equal to 10% of the applied voltage.

3. Breakdown processes with an auxiliary electrode

As a point of departure, the starting of a lamp having an auxiliary electrode will be investigated. The quartz discharge tube, schematically shown in figure 1(*a*), is 2 cm in diameter at its widest with the main electrodes separated by 4 cm. The electrodes are 1 mm in diameter with windings 2.5 mm in diameter. An auxiliary electrode is displaced from the cathode (lower electrode) by 1.8 mm at closest approach. In an actual lamp, the trigger electrode is on one side of the lower electrode. As this is a two-dimensional simulation, this asymmetric geometry cannot be fully resolved, and so we used a cylindrical coordinate system in which the trigger electrode appears as a ring. The ground plane is coaxial and approximately 5.4 cm in diameter. The base-case conditions are a gas fill of argon at 70 Torr with 35 mTorr of Hg, corresponding to its vapour pressure at room temperature. The initial electron and ion densities are zero. Seed electrons are provided by electric field emission, for which we specify a local electric field enhancement due to roughness, approximately 600, at a single mesh point at the tip of the auxiliary electrode. This factor was chosen to provide a critical number of seed electrons during the trigger pulse. Its value is only relevant in that the local electric field enhancement should be large enough to provide seed electrons.

The reaction mechanism employed is shown in table 1. For computational expediency, a single excited state of Ar, nominally Ar(4s), and a single excited state of Hg, nominally Hg(6p), are used. Electron impact on Ar produces Ar(4s) and Ar^+. Multi-step ionization of Ar(4s) is not a major source of Ar^+ during the avalanche when the densities of both electrons and Ar(4s) are not large. The production of Ar_2^+ from

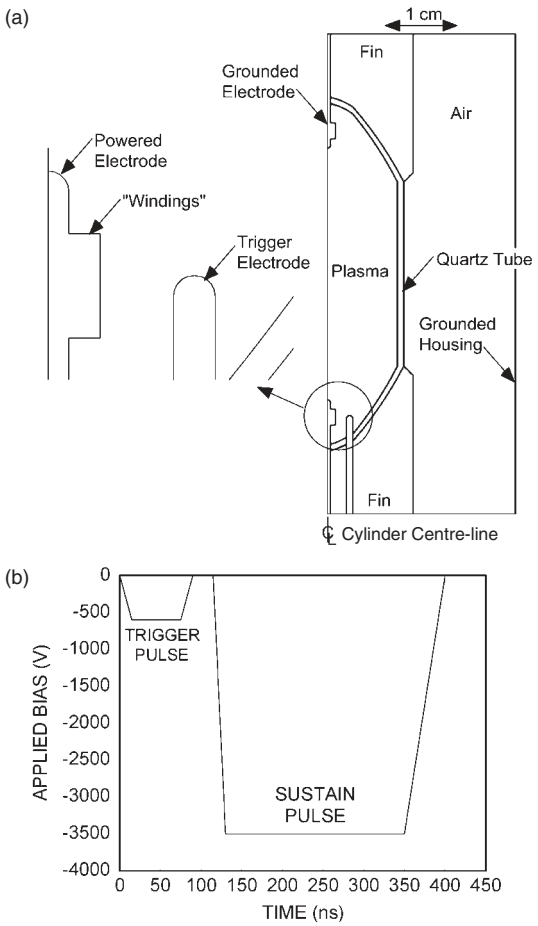

Figure 1. Parameters for the base case: (*a*) schematic of the model geometry and (*b*) voltage waveforms. The cylindrically symmetric HID lamp has an internal trigger electrode. The part labelled 'fin' is the press seal used to make the hermetic seal around the electrodes.

Ar^+ has a lifetime of approximately 1 μs at 70 Torr, and so the majority of Ar ions are the monomers. The resonance radiation from Ar(4s) is virtually totally trapped, with an estimated radiative lifetime of 0.1 s [29] at 70 Torr. As a result the disposition of Ar(4s) excited states is determined almost totally by transport and collisional processes. The trapped resonance radiation does, however, produce photo-ionization of Hg. As discussed below, the quenching of Ar(4s) by Hg, primarily by Penning reactions, produces a lifetime of tens of nanoseconds. Electron impact on Hg directly produces Hg(6s) and Hg^+. At the low vapour pressures of Hg considered here, the Hg dimers, produced by all processes, have small densities and so were not included.

The voltage waveform for the base case, shown in figure 1(*b*), is first a pulse of −600 V (90 ns long with rise and fall times of 15 ns) applied to the trigger electrode, while the cathode and anode are held at ground. After a 35 ns wait, a −3500 V sustain pulse is applied to the cathode and trigger electrode (285 ns long, rise time 15 ns, fall time 50 ns), while the anode is held at ground. These pulse times are shorter than those used in commercial lamps which, depending on the product, could be many to tens of microseconds, and were chosen, in part, for computational expediency. The trends

Table 1. Ar/Hg reaction mechanism: the species involved are e, Ar, $Ar^*(4s)$, Ar^+, Ar_2^*, Ar_2^+, Hg, $Hg^*(6p)$ and Hg^+.

Reactions	Rate coefficient[a]	Ref.
$e + Ar \rightarrow Ar + e$	b	[21]
$e + Ar \rightarrow Ar^* + e$	b	[22]
$e + Ar^* \rightarrow Ar + e$	b, c	[22]
$e + Ar \rightarrow Ar^+ + e + e$	b	[23]
$e + Ar^* \rightarrow Ar^+ + e + e$	b	[24]
$e + Ar^+ \rightarrow Ar^*$	$4.0 \times 10^{-13} T_e^{-0.5}$	[25]
$e + e + Ar^+ \rightarrow Ar^* + e$	$5.0 \times 10^{-27} \times T_e^{-4.5}$ cm^6 s^{-1}	[25]
$e + Ar_2^* \rightarrow Ar_2^+ + e + e$	$9 \times 10^{-8} T_e^{0.7} \times \exp(-3.66/T_e)$	[26]
$e + Ar_2^* \rightarrow Ar + Ar + e$	1×10^{-7}	[26]
$e + Ar_2^+ \rightarrow Ar^* + Ar$	$5.38 \times 10^{-8} T_e^{-0.66}$	[26]
$e + Hg \rightarrow Hg + e$	b	[18]
$e + Hg \rightarrow Hg^* + e$	b	[18]
$e + Hg^* \rightarrow Hg + e$	b,c	[18]
$e + Hg \rightarrow Hg^+ + e + e$	b	[18]
$e + Hg^* \rightarrow Hg^+ + e + e$	b	[27]
$e + Hg^+ \rightarrow Hg^*$	$4.0 \times 10^{-13} T_e^{-0.5}$	[23][d]
$e + e + Hg^+ \rightarrow Hg^* + e$	$5.0 \times 10^{-27} \times T_e^{-4.5}$ cm^6 s^{-1}	[25]
$Ar^* + Ar^* \rightarrow Ar^+ + Ar + e$	5×10^{-10}	[26]
$Ar_2^* + Ar_2^* \rightarrow Ar_2^+ + Ar + Ar + e$	5×10^{-10}	[26]
$Ar^+ + Ar \rightarrow Ar + Ar^+$	4.6×10^{-10}	[28][e]
$Ar^* + Ar + Ar \rightarrow Ar_2^* + Ar$	1.14×10^{-32} cm^6 s^{-1}	[26]
$Ar^+ + Ar + Ar \rightarrow Ar_2^+ + Ar$	2.5×10^{-31} cm^6 s^{-1}	[26]
$Ar_2^* \rightarrow Ar + Ar$	6.0×10^7 s^{-1}	[26]
$Ar^* \rightarrow Ar$	10 s^{-1}	[29][f]
$Ar^* + Hg \rightarrow Hg^+ + Ar + e$	5×10^{-10}	[30]
$Ar^* + Hg^* \rightarrow Hg^+ + Ar + e$	5×10^{-10}	[30][d]
$Ar_2^* + Hg \rightarrow Hg^+ + Ar + Ar + e$	1×10^{-10}	[30][d]
$Ar_2^* + Hg^* \rightarrow Hg^+ + Ar + Ar + e$	1×10^{-10}	[30][d]
$Ar^+ + Hg \rightarrow Hg^+ + Ar$	1.5×10^{-11}	[31]
$Ar^+ + Hg^* \rightarrow Hg^+ + Ar$	1.5×10^{-11}	[31][d]
$Ar_2^+ + Hg \rightarrow Hg^+ + Ar + Ar$	1×10^{-12}	[31]
$Ar_2^+ + Hg^* \rightarrow Hg^+ + Ar + Ar$	1×10^{-12}	[31][d]
$Hg^+ + Hg \rightarrow Hg + Hg^+$	1×10^{-9}	d
$Hg^* + Hg^* \rightarrow Hg^+ + Hg + e$	4×10^{-10}	[32][g]
$Hg^* \rightarrow Hg$	1×10^6 s^{-1}	[29][f]
$h\nu + Hg \rightarrow Hg^+ + e$	5×10^{-15} cm^2	f
$M^+ \rightarrow$ wall $\rightarrow M$	h	
$M^* \rightarrow$ wall $\rightarrow M$	h	

[a] Rate coefficients have units of cm^3 s^{-1} unless mentioned otherwise. Electron temperatures, T_e, are in eV.
[b] The rate coefficient was obtained by solving Boltzmann's equation for the EED. Cross sections for the process are from indicated reference.
[c] Cross section and rate coefficient obtained by detailed balance.
[d] Approximated by analogy.
[e] Determined from mobility of ion in Ar.
[f] See text.
[g] Reaction product is actually Hg_2^+ (associative ionization). To simplify the reaction mechanism, the monomer ion was used as the ionization product.
[h] In wall reactions, all ions recombine to their neutral counterparts and all excited states quench to the ground state.

discussed here are, nevertheless, representative of breakdown processes encountered in typical lamps.

A time sequence of the electron density is shown in figure 2 for the base-case conditions. Following production of seed electrons by electric field emission (approximately 10^3 cm^{-3} at 12 ns) during ramp-up of the trigger pulse (21 ns), electron avalanche occurs between the trigger electrode and the cathode. An electron density of $\approx 10^{11}$ cm^{-3} is produced by the end of the trigger pulse (90 ns). The electron temperature is maximum at approximately 4.7 eV near the windings of the cathode and the tip of the trigger electrode where electric field enhancement is the largest. During the short interpulse period, the electrons diffuse throughout the inter-electrode space and a small electron density ($<10^8$ cm^{-3}) diffuses into the vicinity of the cathode tip (120 ns).

Upon application of the sustain pulse, electron avalanche occurs from the tips of both the trigger electrode and the cathode (140 ns). The avalanche from the cathode is largely initially directed towards the anode, while the avalanche from the trigger tip is initially directed towards the quartz tube. While the electron density is small and electric field deformation is nominal, each of the avalanches follows the direction of the local electric fields, which resemble the vacuum fields. Prior to plasma filling the volume of the tube, the inner walls are not charged, and so electric field lines are directed towards ground planes through the dielectric walls. The avalanching plasma is therefore directed towards the walls (185 ns). As the walls of the discharge tube charge, the external ground plane is shielded from the plasma, redirecting electric field lines towards the anode. Equivalently, one can think of the capacitance of the sidewalls charging, raising the surface potential to that of the local plasma and reducing the electric field perpendicular to the dielectric surface. This process is analogous to the charging of the dielectric surface in pulsed dielectric-barrier-discharges [33]. As the capacitance of the sidewalls charges from the bottom of the tube to the top, the electric field lines are progressively turned upwards, and the plasma walks up the sidewall towards the anode (260 ns). The plasma is then sustained by the large electric fields at the interface of the plasma and non-ionized regions.

As the plasma fills the tube, the voltage division between the more conductive lower portion of the tube and the upper portion of the tube increases the electric field in the low conductivity region, as shown in figure 3, thereby increasing the rate of avalanche. The electron temperature at the leading edge of the avalanche front is 4.2–4.7 eV, while that behind the front where the conductivity is larger is 3.0–3.5 eV. This is a phenomenon similar to that of high pressure stream propagation [34–36]. Photo-ionization produces seed electrons in advance of the avalanche front. If the electric field is sufficiently large, these seed electrons will avalanche. This effect is particularly dramatic near the anode tip. The vacuum electric field at the tip of the electrode at the beginning of the sustain pulse is <20 Td (1 Td $= 10^{-17}$ V cm^2), insufficient to produce an avalanche. As the sustain potential is 'compressed' at the top of the tube due to the increasing conductivity at the bottom of the tube, the E/N at the anode tip increases to nearly 500 Td. When the avalanche front approaches the anode, seed electrons produced by photo-ionization quickly avalanche in this large field, generating a cathode directed avalanche front (see frame for 295 ns in figure 2).

In studies of similar lamps using a one-dimensional model, Pitchford *et al* [37] found that the characteristics of the plasma during the sustain pulse (the takeover pulse in Pitchford's terminology) critically depend on the electron density produced by the initial breakdown pulse (our trigger pulse) and the value of the ballast resistor. Although these quantities were not systematically parametrized here,

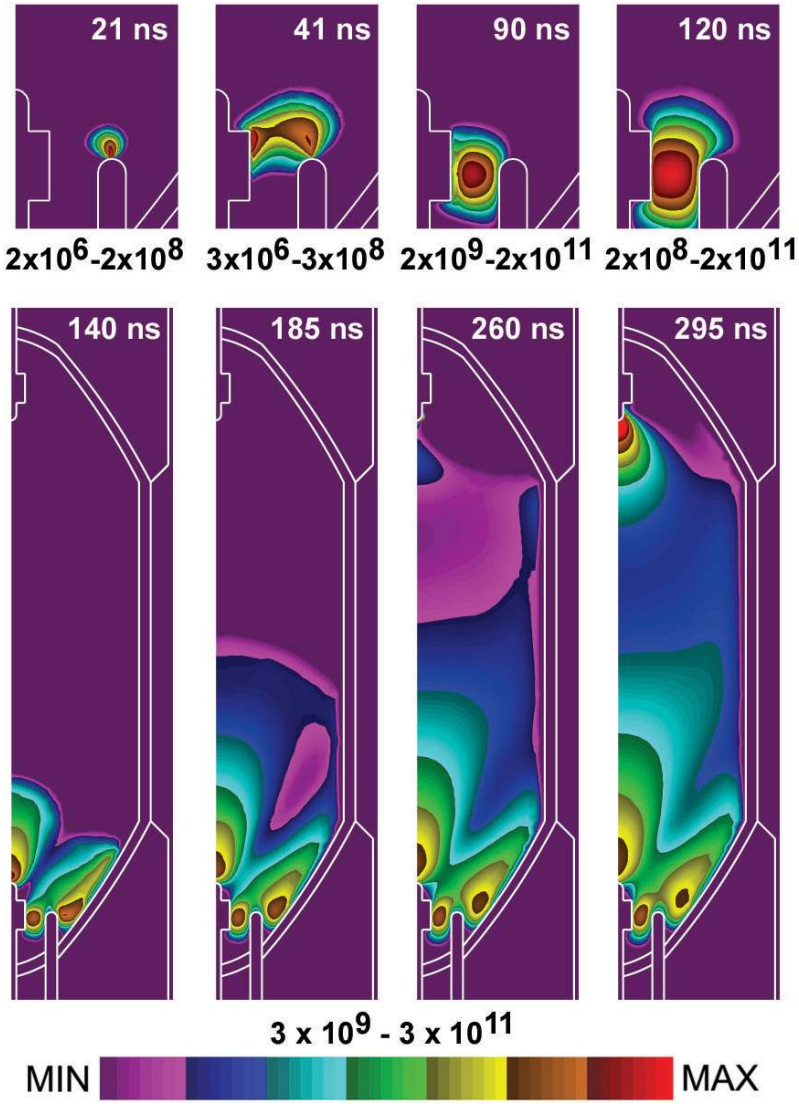

Figure 2. Electron density during start-up of the model HID lamp for the base-case conditions (Ar 70 Torr, Hg 35 mTorr, −3500 V sustain pulse). The frames in the top row are a close-up of the trigger electrode and cathode during the trigger pulse. The frames in the bottom row are for the electron density during the sustain pulse. The range of electron density (log-scale, cm^{-3}) that is plotted is noted below each frame. Secondary electron emission from the trigger electrode initiates the pre-ionization during the trigger pulse. Avalanche of the main gap is initially towards the uncharged walls.

in less formal studies we found that the avalanche time (or equivalently, the minimum breakdown voltage for a fixed sustain period) generally increased as either the voltage or the length of the trigger pulse decreased. There was also a dependence on the length of time between the end of the trigger pulse and start of the sustain pulse. A finite interpulse period is often beneficial to allow diffusion of the plasma to regions where the E/N will be large upon application of the sustain pulse.

The degree to which the avalanche front is Townsend-like or streamer-like [34–36] is in part indicated by the amount of charge density and electric field enhancement that occurs at the front of the avalanche. For example, the positive and negative charge densities early and late during the avalanche for the base-case conditions are shown in figure 4. Positive space charge is indicative of conventional Townsend avalanche or sheath formation. Negative space charge is indicative of streamer-like avalanche (for the anode directed streamer) or dielectric charging. Early during the avalanche (170 ns) positive space charge surrounds the trigger electrode and cathode as conventional glow regions are developing and cathode-fall-like structures are produced. At the front of the avalanche, the space charge is negative, implying streamer-like propagation. Some residual negative space charge remains from the initial electric field emission. Note the negative charging of the dielectric walls in the wake of the avalanche front. Later in the avalanche (275 ns), when the plasma has breached the gap, the sidewall is fully negatively charged. The cathode directed avalanche front originating at the anode is a region of dominantly positive space charge, and so results from Townsend-like processes akin to a conventional glow discharge.

The average E/N across the gap for the base-case conditions is 40 Td. Field enhancement around the tips of the

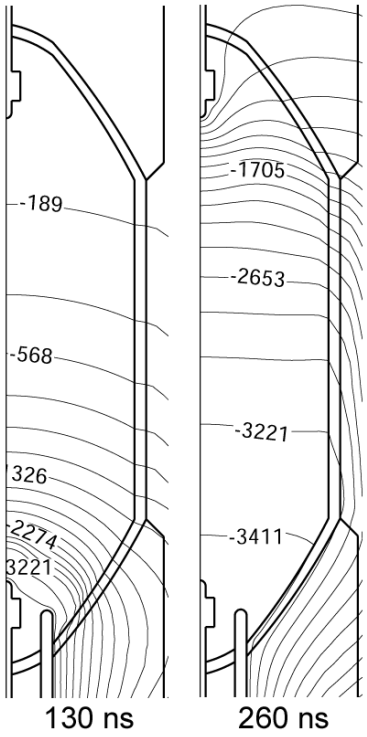

Figure 3. Electric potential (as given by the contour labels) early (130 ns) and late (260 ns) during the sustain pulse for the base-case conditions (Ar 70 Torr, Hg 35 mTorr, −3500 V sustain pulse). Early during the sustain pulse, the electric potential does not differ significantly from its vacuum configuration. As the avalanche increases conductivity near the cathode, the potential is compressed in the upper part of the tube, producing electric field enhancement around the anode.

electrodes may increase this E/N by a factor of two to initiate avalanche. However, to sustain avalanche in the centre of the lamp, some manner of electric field enhancement is required. This enhancement is, in the manner of streamer propagation, provided by space charge separation. The voltage drop behind the avalanche front is small due to the high conductivity plasma produced by the avalanche (low E/N) resulting in the remaining voltage being 'compressed' in front of the avalanche front (large E/N). The dynamics of ionization of the propagating ionization front are therefore different from those behind the front.

These dynamics are shown in figure 5 where the total ion density, E/N and the fraction of ions that are Hg^+ are plotted for different times during the starting of a warm lamp (Hg vapour pressure 70 mTorr or a mole fraction of 0.1%). The conditions are otherwise the same as for the base case. At the beginning of the sustain pulse (130 ns) avalanche begins in the high E/N regions near the tips of the cathode and trigger electrode, with the latter directed towards the wall. Ion densities are $10^8\,cm^{-3}$ at the leading edge of the front and 10^{10}–$10^{11}\,cm^{-3}$ in the plasma behind the front. At the leading edge of the avalanche front, electric field enhancement increases the E/N to 140–150 Td. In spite of the lower ionization potential of Hg, the large E/N (Ar^+ ionization rate coefficient at 150 Td is $2.6 \times 10^{-10}\,cm^3\,s^{-1}$) and large Ar mole fraction results in the initial ionization producing a plasma composed of dominantly $Ar^+(f(Hg^+) < 5$–$10\%)$. As the avalanche progresses up the tube, the wall charges and the E/N at the leading edge somewhat weakens.

At 150 ns, the E/N at the avalanche front is 110 Td. The ionization dynamics behind the front are beginning to convert the dominant ion from Ar^+ to Hg^+. Charge exchange from Ar^+ to Hg^+ has a rate coefficient of $1.5 \times 10^{-11}\,cm^3\,s^{-1}$ producing a mean lifetime for conversion of Ar^+ to Hg^+ of 30 ns. The rate coefficient for Penning ionization of Hg by Ar(4s) is $5 \times 10^{-10}\,cm^3\,s^{-1}$, producing a mean lifetime for conversion of Ar(4s) to Hg^+ of 10 ns. With the lower E/N behind the ionization front (15 Td) producing small rate coefficients for Ar ionization ($7 \times 10^{-16}\,cm^3\,s^{-1}$) and moderate rate coefficients for ionization of Hg ($5.3 \times 10^{-10}\,cm^3\,s^{-1}$) the dominant ion begins to change from Ar^+ to Hg^+.

These trends continue as the avalanche front nears the anode (205 ns). The E/N in the avalanche front weakens, the E/N behind the front decreases while that ahead of the front increases. The fraction of Hg^+ exceeds 50% behind the avalanche front. As photo-ionization seeds electrons in the high E/N near the anode tip, produced by voltage compression, avalanche begins when the E/N exceeds about 50 Td. By the time the plasma closes the gap (250 ns), Hg^+ has become the major ion in the bulk plasma. However, in the cathode directed ionization front emanating from the anode, the E/N is large enough that Ar^+ is the dominant ion, as was the case in the initial stages of the anode-directed avalanche front.

The steady state operating regime of an HID lamp is a nearly local thermodynamic equilibrium (LTE) arc having core temperatures of many thousands of kelvin and pressures of many to tens of atmospheres, and is sustained by thermionic emission from the cathode. When the current is interrupted, the cathode cools and plasma recombines on timescales which are short compared to the time required for the gases (and lamp tube) to cool and metal halide vapours to condense. Restarting of lamps during this cooling period is problematic as the voltage available from the power supply may not be sufficient to provide an avalanching E/N with these high gas densities. To investigate these processes, starting of cold (zero Hg vapour pressure) to warm lamps (Hg vapour 7.8 Torr) were investigated for cold Ar fills of 70 Torr. The conditions are otherwise the same as the base case.

Electron densities at 270 ns for Hg vapour pressures of 0, 70 mTorr, 710 mTorr and 7.8 Torr are shown in figure 6. The time at which breakdown occurs is shown in figure 7. The pure Ar discharge has a breakdown time of 350 ns and the plasma fairly uniformly fills the tube. As small amounts of Hg are added (up to 2.2 Torr, or mole fraction of 0.03) the avalanche time decreases, as this composition is a Penning mixture. Small amounts of the lower ionization potential Hg increase direct ionization rates and produce secondary electrons through Penning ionization. As the Hg pressure exceeds 2–3 Torr, the breakdown time increases, as the larger momentum transfer collision frequency with Hg, which lowers the electron temperature, is not compensated for by the additional ionization generated by Penning processes. For the base-case voltage waveform, breakdown did not occur for pressures of Hg exceeding 10–15 Torr. As the Hg pressure increases, the plasma becomes more nonuniform, with the avalanche being dominantly located along the walls at intermediate pressures.

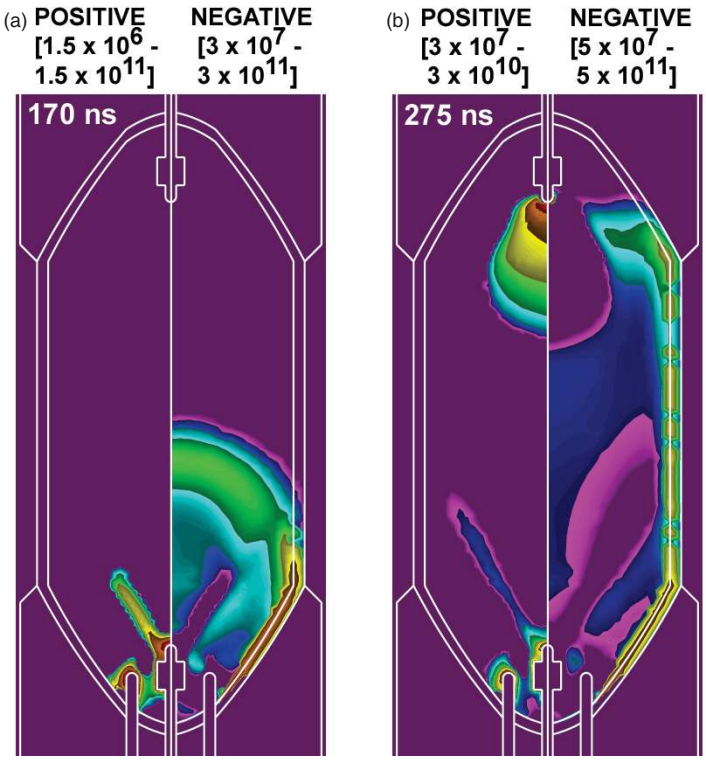

Figure 4. Positive and negative space charge (*a*) early (170 ns) and (*b*) late (275 ns) during the sustain pulse for the base-case conditions (Ar 70 Torr, Hg 35 mTorr, −3500 V sustain pulse). Negative space charge in the anode directed avalanche front indicates a streamer-like propagation of the avalanche. The cathode directed avalanche appears more Townsend-like.

4. Starting of lamps in the proximity of ground planes

The proximity of the ground plane to the discharge tube wall is important in determining both the local electric fields during avalanche and the capacitance of the sidewall. The former is important in determining the path the avalanche takes between the cathode and the anode. The latter is important in determining the intensity of the initial avalanche. One method to control the proximity of the ground plane is by the use of trigger wires wrapped around the exterior of the lamp, effectively making a transient capacitive discharge. Although issues related to loss of sodium through lamp walls may preclude the practical use of permanently mounted trigger wires [7], the dynamics of such a system are illustrative of capacitively dominated breakdown processes. To this end, three lamp meshes were developed using the same basic structure as the base case but without the internal trigger electrode. The lamps have, respectively, no exterior trigger wire; and one winding and three windings of an external trigger wire, as shown in figure 8. The ground planes of the outer housing were removed to sufficient distance (>10 cm) that the discharge appears to be point-to-point without the trigger wires (i.e. electric field lines directed solely between the electrodes). The voltage waveform is a 60 ns ramp from 0 to −3500 V on the cathode, a sustain pulse until 375 ns and a ramp to 0 V at 400 ns.

Electron densities in the three lamps at 65, 150 and 220 ns are shown in figure 9. The magnitude of the charge density in the vicinity of the wall is also shown for the three-trigger wire case. In the absence of the trigger wires, breakdown is not achieved. Avalanche occurs in the vicinity of the cathode tip and the windings on the side of the cathode (65 ns). However, beyond the region of geometrical field enhancement, the E/N is insufficient to sustain the avalanche (30 Td at mid-tube) and, at best, the plasma drifts upwards (150, 220 ns) without significant multiplication. With a single exterior trigger wire, the early avalanche (65 ns) resembles that without the trigger wire. However, the proximity of the ground plane near the trigger wire increases E/N to 60 Td within a few millimetres of the wire compared to 25 Td in its absence. Avalanche occurs in the vicinity of the trigger wire in the manner of a capacitive discharge (150 ns). Avalanche continues until the dielectric is charged, thereby reducing the local E/N to <15 Td (220 ns) which stalls the avalanche at mid-tube.

With three exterior trigger wires, the initial avalanche (65 ns) is more rapid due to the larger E/N (150 Td) afforded by the adjacent trigger wire. A capacitive discharge occurs, which charges the wall of the tube, as shown in the right column of figure 9, and advances the avalanche front. As the avalanche front approaches, compressing voltage in front of it, the local E/N adjacent to the second wire increases to more than 120 Td, thereby advancing the avalanche (150 ns). As the dielectric charges, the local E/N decreases. The process repeats itself in the vicinity of the third trigger wire, as the avalanche boot-straps itself up the sidewall. Sufficient voltage is eventually compressed into the vicinity of the anode tip to create a large enough E/N to launch the cathode directed avalanche.

The proximity of the ground plane and its importance in lamp starting has been recognized in commercial lamps and the patent literature [38]. The ground plane is typically controlled

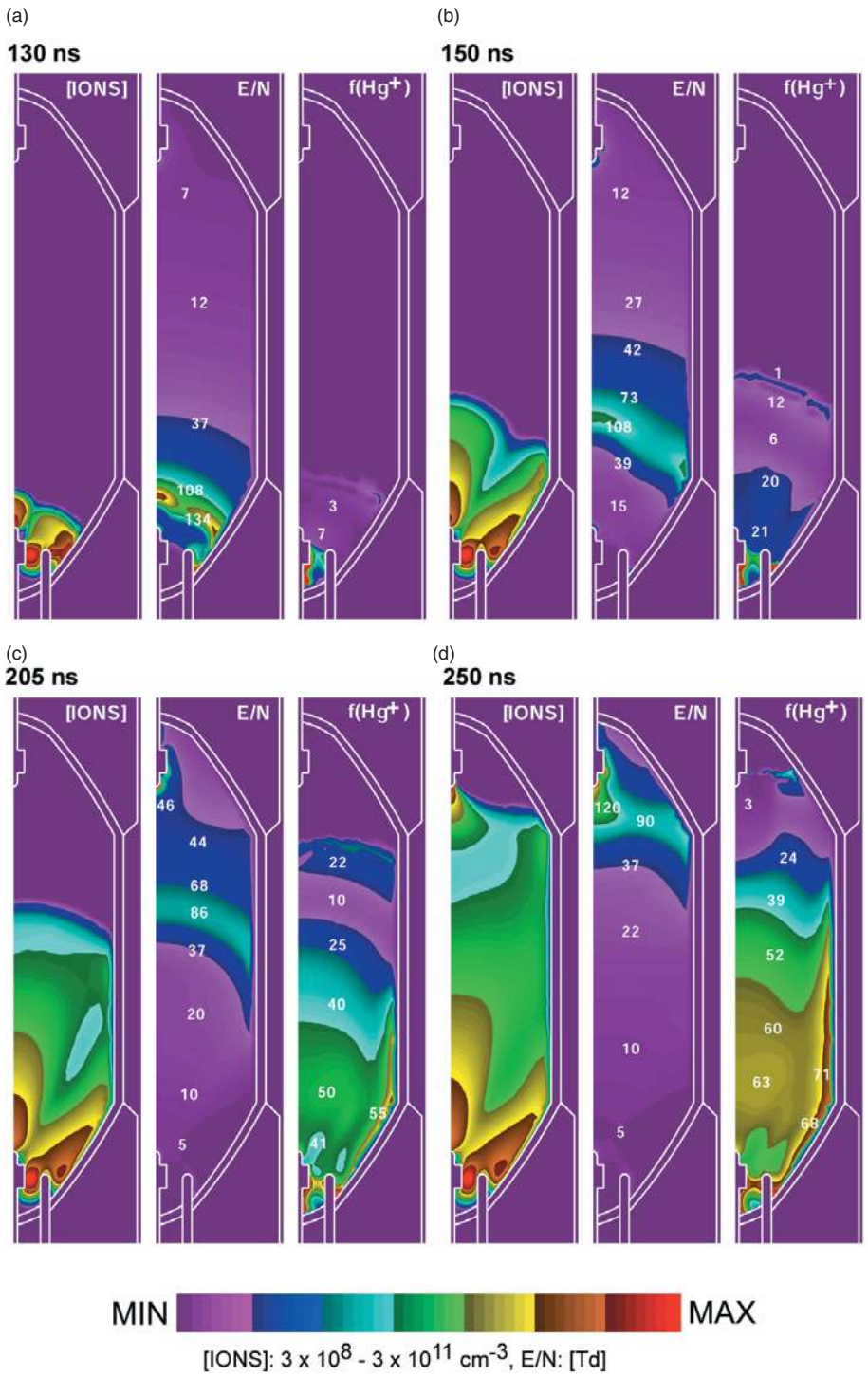

Figure 5. Total ion density (Ar^+ and Hg^+), E/N and fraction of ions which are Hg^+ for a warm lamp (Hg 70 mTorr) for otherwise the base-case conditions (Ar 70 Torr, −3500 V sustain pulse). (*a*) 130, (*b*) 150, (*c*) 205 and (*d*) 250 ns. The ion density has a range of 3×10^8–3×10^{11} cm^{-3}. The labels on the E/N and fraction Hg^+ frames are in Td and per cent, respectively. Electric field enhancement at the front of the avalanche dominantly produces Ar ionization. Charge exchange and Penning ionization behind the avalanche front change the dominant ion to Hg^+.

through the use of a current return wire which is placed an optimized distance from the lamp wall. We investigated this scaling by constructing a two-dimensional asymmetric mesh using Cartesian (as opposed to cylindrical) coordinates having dimensions similar to that of a commercial lamp and with the ground return wire positioned at various distances from the lamp wall, as shown in figure 10. The arc tube has the same dimensions as in the base case. Using the base-case conditions and voltage waveform, breakdown voltages were determined as a function of distance between the wall of the plasma tube and the ground wire at mid-tube. The breakdown voltage was determined by choosing a sustain voltage, running the

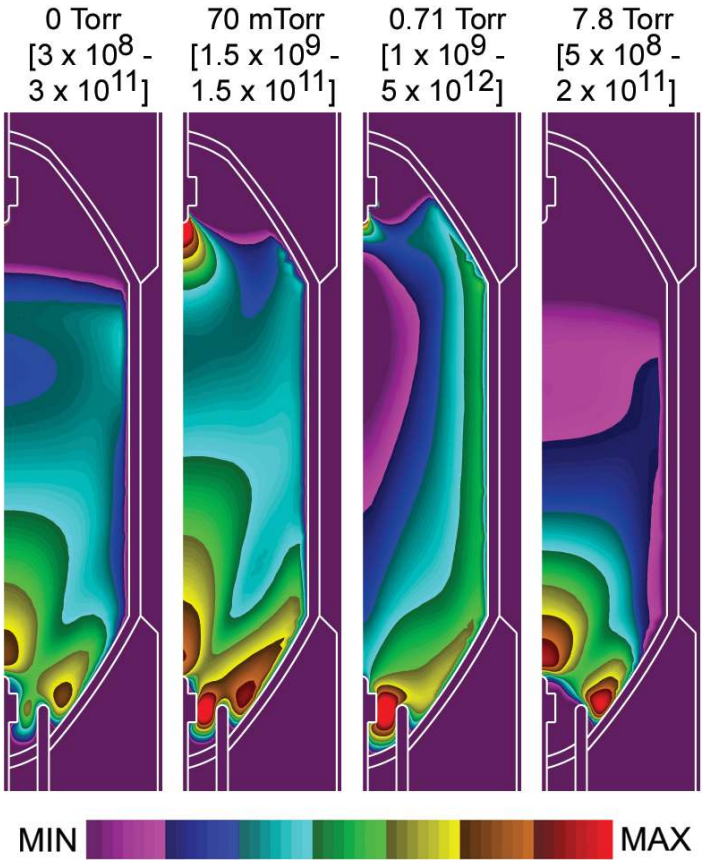

Figure 6. Electron density at 255 ns for cold (0 Torr Hg) to warm (7.8 Torr Hg) lamps for otherwise the base-case conditions (Ar 70 Torr, −3500 V sustain pulse). The range of electron density (log-scale, cm^{-3}) plotted is noted above each frame. At intermediate pressures of Hg, the plasma is dominantly sustained near the wall where the transient capacitive discharge is most intense.

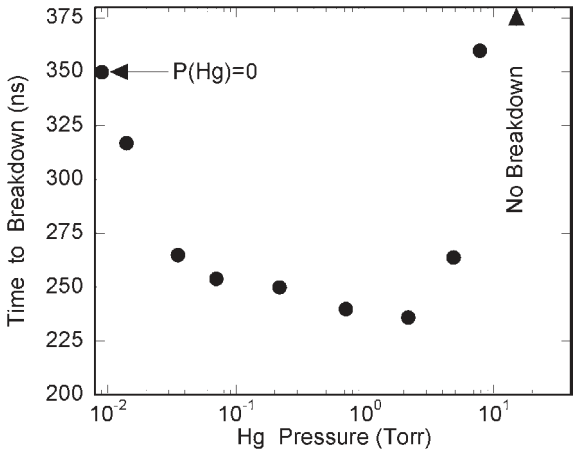

Figure 7. Time to breakdown for cold to warm (0 Torr Hg) to warm (15 Torr Hg) lamps for otherwise the base-case conditions (Ar 70 Torr, −3500 V sustain pulse). Small admixtures of Hg create Penning-like discharges with more rapid breakdown than in pure Ar. At sufficiently high Hg vapour pressure, breakdown does not occur during the sustain pulse due to the larger rate of electron momentum transfer due to the Hg atoms.

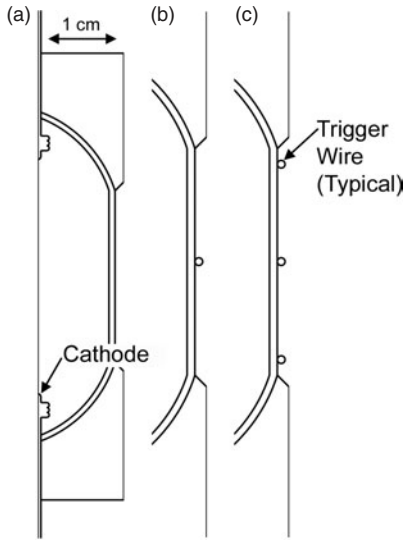

Figure 8. Geometries for breakdown investigation with capacitive trigger wires: (*a*) no trigger wires, (*b*) one trigger wire, (*c*) three trigger wires.

case and seeing if breakdown occurred. If not, the sustain voltage was made more negative and the trial repeated until breakdown did occur. The results are shown in figure 10. Electron densities at three different times during the avalanche for a close (0.6 cm), intermediate (1.5 cm) and far (3.7 cm) spacing between the wall and ground return wire are shown in figure 11.

The larger E/N and more intense capacitively sustained avalanche afforded by the closer proximity of the ground wire enable lower breakdown voltages, here decreasing the

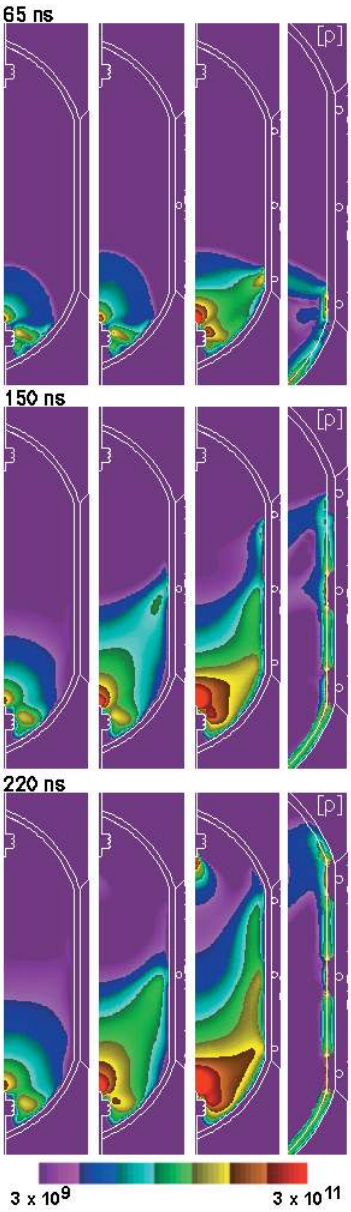

Figure 9. Electron density at 65, 150 and 250 ns for the lamp geometries shown in figure 8 which have none, one and three external trigger wires. The base-case conditions were used (Ar 70 Torr, 35 mTorr Hg, −3500 V sustain pulse) except that the sustain pulse begins at $t = 0$. The range of electron density (log-scale) is 3×10^8–3×10^{11} cm^{-3}. The absolute value of the charge density ρ (2.6×10^8–2.6×10^{12} cm^{-3}) is shown in the enlarged frame at the right. The external trigger wires provide for a transient capacitive discharge which boot-straps the avalanche front up the side of the discharge tube.

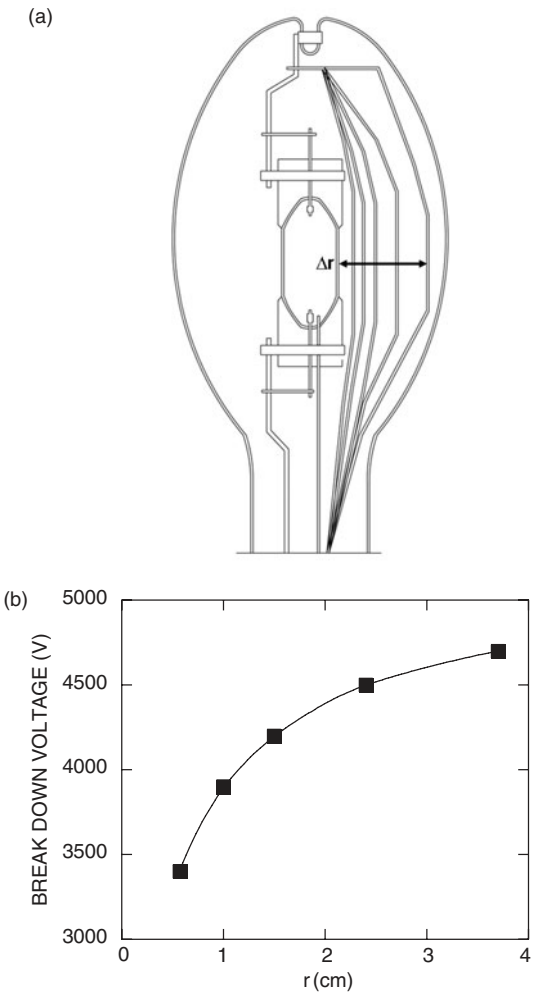

Figure 10. Consequences of the location of the current return wire on breakdown voltage. (*a*) Positions of the current return wire. The discharge tube has the same dimensions as shown in figure 1. (*b*) Breakdown voltage as a function of distance of the return wire from the discharge tube wall. The conditions are Ar 70 Torr, Hg 70 mTorr and the base-case voltage waveform. Close proximity of the wire provides for a more intense capacitive discharge and more rapid breakdown.

voltage from 4700 to 3300 V. The dynamics and symmetry of the avalanche are similarly affected. The close proximity of the ground wire produces a highly asymmetric discharge which, in the extreme, could produce enhanced wall erosion. As the ground return wire extends further from the discharge tube, the avalanching plasma forms in a more uniform fashion. However, the reduced capacitance and lower E/N which results is inefficient in advancing the avalanche front.

The actual lamps being modelled clearly have three-dimensional character which may produce quantitatively different results from those discussed here. Consider the two-dimensional cylindrically symmetric lamps with trigger electrodes discussed in section 3. Trigger electrodes are not annular discs, as represented in the two-dimensional model, but are rather discrete posts. One consequence of this approximation is that electric field enhancement in the vicinity of the trigger electrodes will be greater in three dimensions, thereby producing more rapid avalanche. This effect may be counter balanced by the lower amount of current produced by the smaller post trigger electrode, which would likely produce less rapid gap closure. For example, the capacitance of the side wall will charge slower, thereby lengthening the time required for the electric field lines to be redirected towards the anode. The trigger electrodes are inherently asymmetric, and as a result actual lamps have breakdown asymmetries as discussed in this section. Although these asymmetries are captured by their Cartesian two-dimensional representation, there are still intrinsic approximations. For example, the electrodes in the Cartesian two-dimensional mesh appear as finite thickness

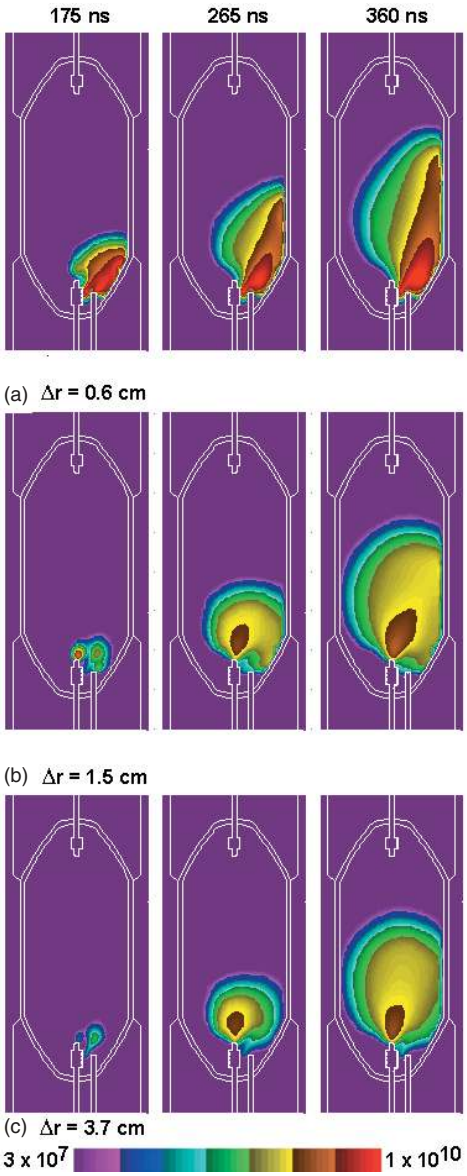

Figure 11. Electron density at 175, 265 and 365 ns for the conditions of figure 10 (Ar 70 Torr, Hg 70 mTorr) for separations between the lamp and the current return wire of (*a*) 0.6, (*b*) 1.5 and (*c*) 3.7 cm (see figure 10(*a*)). The range of the electron density (log-scale) is 3×10^7–1×10^{10} cm^{-3}. The close proximity of the ground wire produces a more intense and asymmetric capacitive discharge, which enables more rapid avalanche.

'slabs' (into the unresolved third dimension) as opposed to cylindrical posts. As a result, the electric field enhancement at their tips is smaller than in the real lamp, producing less rapid avalanche. The general scaling laws developed through our investigation should, in large part, extend to three dimensions, as they are based on fundamental phenomena. Having said that, as demonstrated here, subtle geometrical differences can have large effects on quantitative behaviour.

5. Concluding remarks

A model for breakdown processes in HID lamps has been described and parametric results have been discussed while considering restart of warm lamps, and the use of internal and external trigger wires. The start-up of cold lamps is sensitive to the transient capacitive discharge, which results from the proximity of ground planes adjacent to the walls of the tube. To avalanche with moderate applied voltages, the ground plane must be sufficiently close that an avalanche capable E/N is produced, and a critically large capacitance is required to generate enough charge density to enable the avalanche front to progress. Avalanche into previously non-ionized gas proceeds from cathode to anode with mechanisms similar to those of streamer propagation. The return, cathode directed avalanche through previously ionized gas advances dominantly through a Townsend-like mechanism. Small mole fractions of Hg (less than a few per cent), as might be present during start-up of a warm lamp, increase the rate of avalanche and reduce breakdown voltages by providing a Penning mixture with the buffer gas. Further increasing the mole fraction of Hg increases the rate of electron momentum transfer (thereby decreasing the electron temperature and excitation rates) to the extent that the advantages of the Penning mixture are lost. Breakdown is then more difficult to achieve.

Acknowledgments

This work was supported by the General Electric R&D Center and the National Science Foundation (CTS 99-74962). The authors would like to thank Drs Timothy Sommerer and David Wharmby for their guidance during this investigation.

References

[1] Zaslavsky G, Cohen S and Keeffe W 1990 *J. Illum. Eng. Soc.* **19** 76
[2] Byszewski W W and Budinger A B 1990 *J. Illum. Eng. Soc.* **19** 70
[3] Cohen S, Zaslavsky G and Lester J N 1989 *J. Illum. Eng. Soc.* **18** 3
[4] Gregor P D, Li Y M, Budinger A B and Byszewski W W 1996 *J. Illum. Eng. Soc.* **25** 150
[5] Byszewski W W, Li Y M, Budinger A B and Gregor P D 1996 *Plasma Sources Sci. Technol.* **5** 720
[6] Pitchford L C, Peres I, Liland K B, Boeuf J P and Gielen H 1997 *J. Appl. Phys.* **82** 112
[7] Waymouth J F 1987 *J. Illum. Eng. Soc.* **16** 166
[8] Luijks G M J F and van Vliet J A J M 1988 *Lighting Res. Technol.* **20** 87
[9] Cifuentes L, Forsdyke G M and O'Brien N W 1992 *Corrosion Sci.* **33** 1581
[10] Fukumori N, Nishimura H, Uchihashi K and Fukuhara M 1995 *J. Illum. Eng. Soc.* **24** 41
[11] Smith D and Zhu H 1993 *J. Illum. Eng. Soc.* **22** 27
[12] Gibson R G 1994 *J. Illum. Eng. Soc.* **23** 19
[13] Skyblue Systems, Inc, PO Box 14223, Albany, NY 12212–4223, http://www.skybluesystems.com
[14] Rauf S and Kushner M J 1999 *J. Appl. Phys.* **85** 3460
[15] Scharfetter D L and Gummel H K 1969 *IEEE Trans. Electron Dev.* **ED-16** 64
[16] SLAP Sparse Matrix Library, http://www.netlib.org
[17] Seager M K 1998 *Lawrence Livermore National Laboratory Technical Report* UCRL-100195, http://www.llnl.gov
[18] Rockwood S D 1973 *Phys. Rev.* A **8** 2348
[19] Steinbruchel C 1989 *Appl. Phys. Lett.* **55** 1960
[20] Dyke W P and Dolan W W 1956 *Advances in Electronics and Electron Physics* ed L Marton (New York: Academic) p 89
[21] Hayashi M 1991 *Nagoya Institute of Technology Report No.* IPPJ-AM-19

[22] Tachibana K 1986 *Phys. Rev.* A **34** 1007
[23] Rapp D and Englander-Golden P 1965 *J. Chem. Phys.* **43** 1464
[24] McFarland R H and Kinney J D 1965 *Phys. Rev.* **137** A1058
[25] Biondi M A 1976 *Principles of Laser Plasmas* ed G Bekefi (New York: Wiley) ch. 4
[26] Kannari F, Obara M and Fujioka T 1985 *J. Appl. Phys.* **57** 4309
[27] Vriens L 1964 *Phys. Lett.* **8** 260
[28] Ellis H W, Pai R Y, McDaniel E W, Mason E A and Viehland L A 1976 *At. Data Nucl. Data Tables* **17** 177
[29] Holstein T 1951 *Phys. Rev.* **83** 1159
[30] Karov M, Rusinov I and Balgoev A 1997 *J. Phys. B: At. Mol. Opt. Phys.* **30** 1361
[31] Johnsen R and Biondi M A 1980 *J. Chem. Phys.* **73** 5045
[32] Klucharev A N and Vujnovic V 1990 *Phys. Rep.* **185** 55
[33] Eliasson B and Kogelschatz U 1991 *Trans. Plasma Sci.* **19** 309
[34] Kulikovsky A A 1998 *Phys. Rev.* E **57** 7066
[35] Georghiou G E, Morrow R and Metaxas A C 1999 *J. Phys. D: Appl. Phys.* **32** 1370
[36] Vitello P A, Penetrante B M and Bardsley J N 1994 *Phys. Rev.* E **49** 5574
[37] Pitchford L C, Peres I, Liland K B, Boeuf J P and Gielen H 1997 *J. Appl. Phys.* **82** 112
[38] Fridrich E G and Bergman R S 1977 Short-arc discharge lamp with starting device *United States Patent* 4 053 809. Filed 18 June 1976; granted 11 October 1977